J Comput Neurosci (2008) 25:317–333
DOI 10.1007/s10827-008-0081-y

Fluctuation-driven rhythmogenesis in an excitatory neuronal network with slow adaptation

William H. Nesse · Alla Borisyuk · Paul C. Bressloff

Received: 14 June 2007 / Revised: 5 January 2008 / Accepted: 25 January 2008 / Published online: 22 April 2008

Abstract We study an excitatory all-to-all coupled network of N spiking neurons with synaptically filtered background noise and slow activity-dependent hyperpolarization currents. Such a system exhibits noise-induced burst oscillations over a range of values of the noise strength (variance) and level of cell excitability. Since both of these quantities depend on the rate of background synaptic inputs, we show how noise can provide a mechanism for increasing the robustness of rhythmic bursting and the range of burst frequencies. By exploiting a separation of time scales we also show how the system dynamics can be reduced to low-dimensional mean field equations in the limit $N \to \infty$. Analysis of the bifurcation structure of the mean field equations provides insights into the dynamical mechanisms for initiating and terminating the bursts.

Keywords Noise-induced bursting · Excitatory network · After hyperpolarization (AHP) · Slow adaptation · Mean-field model

1 Introduction

A major area of study in neurobiology is understanding the dynamical mechanisms that underly the production of oscillations (Buzaki 2007). One particularly interesting way rhythmic burst oscillations can arise is through a recurrently connected network of neurons possessing excitatory synapses and slow activity-dependent depression or adaptation (Tabak and Rinzel 2005; Van Vreeswijk and Hansel 2001). Such rhythms have been found in several brain areas including the Pre-Bötzinger complex (PreBotC) (Smith et al. 1991) and the developing chick spinal cord (O'Donovan 1999). In the present work we explore the role of random synaptic fluctuations in modulating rhythmic bursting in an excitatory neuronal network model with slow adaptation. Specifically, we establish the following results: (1) Independent noise input to cells can induce very regular population-level oscillations in the averaged firing rate of the neurons. (2) Noise can increase the parameter range where rhythmic population oscillations exist, while also increasing the available frequency range, thereby making the rhythm generator more robust. (3) Under the assumption that the variability of noise depends on the rate of background synaptic inputs, we illustrate how noise can be an important modifying component to the global network behavior. (4) By performing an analytical reduction of the large spiking network to a mean-field description, we reveal the mechanism of the population burst as a bifurcation in the mean-field model, which we show for two distinct adaptation mechanisms – one a linear, synaptically mediated adaptation, resulting in a Hopf bifurcation, and the other a nonlinear, calcium-mediated adaptation, resulting in a saddle-node on an invariant cycle Rinzel and Ermentrout bifurcation (SNIC). By analyzing the bifurcation structure of these mean-field models, we establish that population-level burst oscillations in excitatory networks can behave analogously

Action Editor: Misha Tsodyks

W. H. Nesse · A. Borisyuk · P. C. Bressloff (✉)
Department of Mathematics, University of Utah,
Salt Lake City, UT 84112, USA
e-mail: bressloff@math.utah.edu

to the Hopf or SNIC classifications of single model neurons (Rinzel and Ermentrout 1998).

The PreBotC is a rhythmogenic network in the mammalian brainstem thought to control the inspiratory phase of breathing (Smith et al. 1991). Cells in the PreBotC exhibit synchronized bursts of action potentials that together form a population-level oscillation with periods on the order from seconds to minutes in a slice preparation (Funk and Feldman 1995). The rhythmogenic PreBotC cells form a synaptically connected network that requires glutamatergic excitatory neurotransmission to create the breathing rhythm (Ge and Feldman 1998). On the other hand, inhibition appears non-essential since the rhythm persists when inhibition is blocked (Brockhaus and Ballanyi 1998; Johnson et al. 2002). Many studies have focused on how intrinsic currents in a minority population of intrinsically rhythmic bursting, so called "pacemaker" cells, could mediate population rhythmicity (Butera et al. 1999a, b; Del Negro et al. 2001; Tryba et al. 2003. More recently, however, there is evidence that pacemaker bursting cells may not be necessary for the production of the population rhythm, and it has been hypothesized that the rhythm is an emergent network property mediated by recurrent excitation (Pace et al. 2007; Feldman and Del Negro 2006; Del Negro et al. 2002).

Developing chick spinal cord is another area where excitatory neurotransmission plays a role in rhythmic burst generation. In this preparation synchronized population burst episodes are observed between silent periods on the order of many minutes. These episodes are thought to be a population-level phenomenon which is terminated through an activity-dependent depression (Chub and O'Donovan 2001; O'Donovan 1999) and mediated through purely excitatory synapses. The absence of inhibition is a consequence of the fact that the chloride reversal potential in the developing nervous system is above the resting potential and therefore GABAergic synapses are excitatory (Cupello 2003; Sernagor et al. 1995).

Modeling studies suggest that emergent synchronized oscillatory network bursting is a generic property of recurrently connected excitatory neuronal networks with slow activity-dependent depression. This type of bursting can induce synchronization at the single spike level as has been shown by Tsodyks et al. (2000) in the case of a network of predominantly excitatory leaky integrate-and-fire (LIF) cells. These cells transiently synchronize and then synaptically depress, effectively decoupling the network until the depression wears off and a population spike recurs. More recently, Loebel and Tsodyks (2002) have shown how this network behavior can be well captured by a low-dimensional mean-field equation representing the population firing rate. Van Vreeswijk and Hansel (2001) have shown similar rhythmic population bursting in LIF model cells coupled to a slow activity-dependent hyperpolarizing current.

Tabak et al. (2000, 2001, 2006) have employed a form of Wilson-Cowan mean-field equations (Wilson and Cowan 1972) to investigate the dynamics of synchronized population bursts in developing chick spinal cord. In this model synchronization occurs at the level of the mean firing rate of each cell rather than at the level of individual spikes. Analysis of the mean-field equations establishes how a burst oscillation mediated by recurrent excitation is terminated by slowly activating synaptic depression, which then slowly deinactivates until the next bursting episode is elicited. Recently, an approximate derivation of the mean-field equations in Tabak et al. (2000) has been carried out for a population of LIF spiking neurons possessing a certain level of disorder, either due to a spatial heterogeneity in the excitability of each cell (as determined by an external bias current) or due to each cell being driven by a small amount of white noise (Vladimirski et al. in press). Analysis of the spiking network dynamics establishes that burst oscillations are more robust in the presence of spatial heterogeneity due to the crucial role of a subpopulation of cells with intermediate excitability, which are able to become active in response to input from more excited subpopulations, thus generating sufficient input onto the remaining less excitable cells to initiate a full population burst. Spatial heterogeneity also appears more effective than white noise in generating spontaneous rhythmic bursting, assuming that the noise is independent of the bias current.

Kosmidis et al. (2004) have explored the role of noise in a computational model of PreBotC consisting of an excitatory network of Hodgkin Huxley neurons. All cells were identical and possessed an activity-dependent calcium-activated potassium current that terminates bursts and intrinsic calcium currents I_L and I_T (high and low threshold activated calcium currents, respectively) that can only produce autonomous bursting in synaptic isolation (i.e. pacemaker activity) with a sufficiently large depolarizing current. The authors show how noise-induced population bursts can occur below the threshold of autonomous pacemaker bursting, with the oscillations persisting over a finite range of white noise current input strengths (variance). The oscillations appear at a critical level of noise, beyond which increasing the noise produces a progressive increase in the burst frequency along with a decrease

in the burst amplitude until bursting stops when the amplitude reaches zero for sufficiently high levels of noise.

Many theoretical studies have focused on how random membrane fluctuations can affect cellular excitability and firing rate (Destexhe et al. 2001; Lindner et al. 2004). In these studies the random current inputs to the excitable cells are taken to be Gaussian white noise or near-white noise processes. White noise inputs can produce coherent spiking in single cells (see Lindner et al. 2004 for a review). In excitable neuronal models such as LIF and relaxation oscillators, it has been found that there is an optimal white noise amplitude, termed coherence resonance (CR), that produces the most regular spiking statistics, usually indicated by the height and sharpness of the power spectrum (Gang et al. 1993; Rappel and Strogatz 1994) and is found to be a generic property of excitable systems possessing fast and slow time scales (Pradines et al. 1999). White-noise-induced oscillations have also been observed at the network level, in which there is an optimal noise strength that causes the most coherent spike–synchronization (Rappel and Karma 1996; Pham et al. 1998; Han et al. 1999). If the network size is made sufficiently large ($N \to \infty$) then the coherence can be described in terms of a deterministic mean-field model (Kurrer and Schulten 1995; Pikovisky and Ruffo 1999). Recently, mean-field equations have also been derived for a large-N excitatory spiking network of VSLI model (non-leaky IF model) cells possessing a slow activity-dependent hyperpolarizing current (AHP) in addition to white noise inputs (Gigante et al. 2007). In this model, noise is set to a fixed value and a population firing-rate is derived via the numerical computation of a truncated set of eigenfunctions for the associated nonlinear Fokker-Planck equation (Mattia and Giudice 2002). Population-level burst oscillations are found to depend on the synaptic coupling and the strength of the AHP but the level of noise itself was not investigated as a control parameter.

Motivated by the above studies we present a systematic analysis of the effects of synaptic noise on the production of rhythmic synchronized bursting in an excitatory network with slow adaptation, where random fluctuations in network activity kindle an ever-increasing excitation leading to a burst; the burst is then terminated by a slow AHP current resulting in a well-defined rhythmic pattern. Note that in this model the burst phenomena is purely network driven. There are no intrinsic voltage-gated currents that autonomously elicit bursting in isolated cells. One main conclusion from this analysis is that Poisson–like synaptic inputs, which cause both noise strength and excitability to increase together, can provide a greater range of burst frequencies compared to the case where no noise is present.

For simplicity, we consider a globally coupled network of N LIF neurons with slow AHP currents and synaptically filtered background noise. We assume that the membrane time constant is fast relative to the synaptic and AHP time scales so that we can reduce the complex spiking model to a firing rate model through short-time averaging. Using stochastic analysis we then reduce the rate–based network equations to a low-dimensional mean field equation in the large-N limit. We show through numerical simulations that the mean-field equations match well the behavior of the full large-N spiking model. We find that the mean-field system exhibits a non-oscillatory, low firing-rate "resting" state for sufficiently weak noise and bias current. The system exhibits oscillations for an intermediate range of noise strengths and input currents as indicated by bifurcation analysis of the mean-field system. The existence of oscillations over this parameter range is analogous to population-level coherence resonance. In this paper we consider two distinct forms of AHP current that both serve the purpose of burst termination, but produce different bifurcation mechanisms to bursting. The first models a linear synaptically activated AHP current in which bursting occurs via a Hopf bifurcation. The second models a nonlinear calcium–dependent potassium current in which bursting occurs via a saddle–node on a limit cycle (SNIC) bifurcation.

While the mechanisms for AHP current activation is quite diverse (e.g. voltage, synaptic, or second-messenger activated, see Hille 2001), the particular AHP schemes are chosen so that (1) isolated cells *do not* exhibit autonomous bursting in the absence of synaptic input, thus showing that the population rhythm is an emergent network-level phenomenon, and (2) reveal that the excitability mechanism of the network system can take the Hopf and SNIC forms analogous to that observed in single-neuron excitability (see Rinzel and Ermentrout 1998). The onset of oscillations through the Hopf mechanism emerge at a finite frequency. On the other hand, SNIC oscillations emerge through a homoclinic cycle, exhibit arbitrarily long periods near the bifurcation, and transient super-threshold inputs can produce arbitrarily long latencies to complete the oscillation. Voltage-gated AHP mechanisms are not studied in the present work because the LIF model is not a realistic model of nerve membrane voltage. However, we postulate that one could construe a voltage-gated AHP model in combination

with a more realistic model of membrane voltage that exhibits network level bursting similar to the two AHP models presently studied. For parsimony, we leave such prospects for another time.

2 Methods

2.1 Derivation of the N-cell spiking network

Consider a globally coupled network of N model neurons labeled $i = 1, \ldots, N$. Each neuron is described by a somatic membrane voltage variable v_i that captures the spiking dynamics of the cell. The membrane voltage receives a synaptic input $s(t)$, a synaptic noise current $x_i(t)$, a bias current I_v, and an activity-dependent hyperpolarization (AHP) h_i current. The voltage is modeled with LIF dynamics as

$$\tau_v \frac{dv_i}{dt} = -v_i + s - h_i + I_v + x_i, \quad v_i < \theta. \tag{1}$$

When v_i is below the spiking threshold θ, the cell has a linear response to the total input $s - h_i + I_v + x_i$. Immediately after firing, v_i is reset to a hyperpolarized level $v_r < 0$ for a refractory time τ_r, during which the cell is held "offline" such that the synaptic inputs and the bias current I_v have no affect on the v_i dynamics. In order for all terms in Eq. (1) to have the same physical units, we assume that the voltage is scaled by a unit resistance.

The synaptic dynamics are modeled as an "alpha" function response to each spike event in the network with time constant τ_s. We denote the list of spike events elicited by the i^{th} cell by $S_i = \{t_j^i\}_{j=1}^{\infty}$. Hence, the synaptic dynamics are

$$\tau_s \frac{ds}{dt} = -s + w \tag{2}$$

$$\tau_s \frac{dw}{dt} = -w + \frac{a_s}{N} \sum_{i=1}^{N} \sum_{j \in S_i} \delta\left(t - t_j^i\right), \tag{3}$$

where a_s is a positive parameter and $\delta(t)$ is the Dirac delta function. For simplicity, we take the network to be homogenous and globally coupled. Thus, each cell in the network receives the same synaptic input $s(t)$. Figure 1 depicts schematically the network setup where the $i = 1 \ldots N$ all-to-all coupled cells produce the population synaptic activity $s(t)$, and an outside neural structure provides randomly fluctuating synaptic currents to the population.

The synaptic noise $x_i(t)$ is modeled as an "alpha" function response to a Poisson input spike train $\mu_i(t) = \sum_j \delta(t - t_j^i)$, where the inputs t_j^i, $j \in \mathbb{Z}$ are statistically

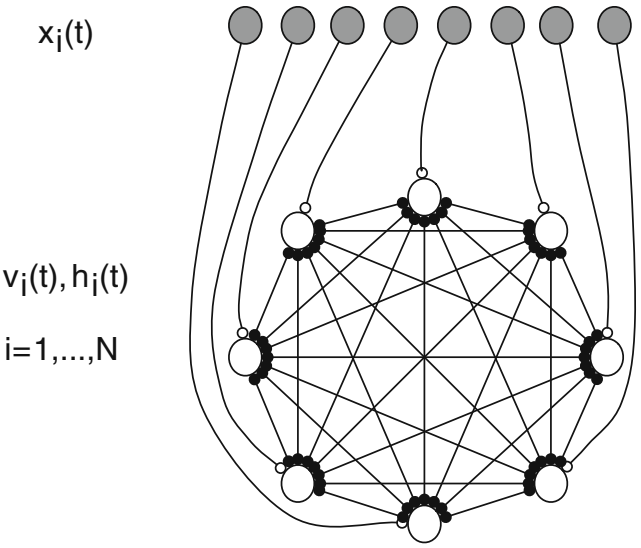

Fig. 1 Schematic diagram of the all-to-all coupled network defined by voltage variables $v_i(t)$ and adaptation variables $h_i(t)$ (and other variables not shown), for $i = 1 \ldots N$ indicated by the lower circular array of *open circles*. The exogenous synaptic input $x_i(t)$ is indicated by the *gray circles* above

independent for each i. We conceive of this synaptic noise as arising outside the network as an exogenous input from other neural sources. Hence, similar to Eqs. (2) and (3), the synaptic kinetics processes the synaptic noise input as

$$\tau_x \frac{dx_i}{dt} = -x_i + y_i \tag{4}$$

$$\tau_x \frac{dy_i}{dt} = -y_i + a_x \mu_i(t), \tag{5}$$

where upon each Poisson event, the y variable is increased by a_x, representing the synaptic strength of the input. Let $q(y, t)$ represent the probability density that $y_i = y$ at time t. The dynamics of this distribution due to the Poisson input can be described by the master equation

$$\tau_x \frac{\partial q(y,t)}{\partial t} = \frac{\partial}{\partial y}\big[yq(y,t)\big] + \nu\big[q(y - a_x, t) - q(y,t)\big], \tag{6}$$

where the first term on the right-hand side of Eq. (6) represents the negative gradient of the probability flux given no spike input occurs, and the second term represents the probability shift of y by a_x at a rate ν that the spike events do occur. If we assume that the input to each cell is weak so that a_x is small, then we can Taylor

expand the second term in Eq. (6) to second order in a_x, leading to the Fokker–Planck equation

$$\tau_x \frac{\partial q(y,t)}{\partial t} = -\frac{\partial}{\partial y}\big[(\nu a_x - y)q(y,t)\big] + \frac{\nu a_x^2}{2}\frac{\partial^2}{\partial y^2}\big[q(y,t)\big] \tag{7}$$

The attracting steady state solution to Eq. (7) is a Gaussian distribution $q(y)$ with mean νa_x and variance $\nu a_x^2/2\tau_x$. The corresponding steady-state probability density for $x_i = x$, which we denote by $p(x)$, is also Gaussian with the same mean but half the variance. This follows from approximating Eqs. (4) and (10) by a multidimensional Ornstein-Uhlenbeck process (see below). Hence, the synaptically driven noise x provides a constant input current νa_x to the membrane voltage equation and a fluctuating part with variance $\sigma^2/4$ where

$$\sigma = \sqrt{\frac{\nu}{\tau_x}}a_x \tag{8}$$

For simplicity, we will absorb the mean current νa_x into the membrane bias current by performing the shift $x \to x - \nu a_x$ and setting

$$I_v = I_0 + \nu a_x. \tag{9}$$

for some fixed background I_0. Under these approximations, we can replace Eqs. (4) and (5) by the multidimensional Ornstein-Uhlenbeck process

$$\tau_x \frac{dx_i}{dt} = -x_i + y_i \tag{10}$$

$$\tau_x \frac{dy_i}{dt} = -y_i + \sigma\sqrt{\tau_x}\xi_i(t) \tag{11}$$

where $\xi_i(t)$ is a white noise process with $\langle \xi_i \rangle = 0$, $\langle \xi_i(t)\xi_j(t')\rangle = \delta(t-t')\delta_{i,j}$.

In this paper we model the noise according to Eqs. (10) and (11) and investigate how rhythmic bursting depends on the level of cellular excitability (as determined by the bias current I_v) and the noise strength σ, both treated as independent parameters. We then apply our results to the particular case of Poisson inputs, for which variation in one of the control parameters ν or a_x generates a natural path through I_v-σ parameter space.

The activity-dependent hyperpolarizing (AHP) current h_i is assumed to have slow kinetics relative to other time scales in the model. Taken together with the aforementioned time-scale separation between soma and synapse, we have $\tau_v \ll \tau_s, \tau_x \ll \tau_h$ where τ_h denotes the time constant for AHP activation. We consider two distinct activating schemes for the AHP current, which differ in their underlying biophysical interpretation and also produce distinct mechanisms for population burst rhythmogenesis (see Section 3). The purpose behind either type of AHP current is that elevated activity, defined in terms of prevalence of spiking or the consequent synaptic activity $s(t)$, will slowly activate the AHP current, thereby depressing the elevated activity. The first scheme is modeled as a synaptically activated AHP current, in which the synaptic inputs $s(t)$ and $x_i(t)$ produce spiking in the voltage equation at a short time scale and slowly activate h_i according to the linear equation

$$\tau_h \frac{dh_i}{dt} = -h_i + a_h(s + x_i), \tag{12}$$

where a_h is a positive constant. This simple activation scheme loosely models the slow kinetics associated with a synaptically activated matabotropic outward current (see Jonas and Kaczmarek 1999, for a review).

The second AHP model we examine possesses a more complicated activation scheme based upon a calcium-activated potassium current. We now assume that each time a cell fires a bolus a_c of calcium enters the cell and the resulting increase in calcium concentration activates the AHP current. Let c_i denote the intracompartmental calcium level of the i^{th} cell. The nonlinear AHP dynamics is then

$$\tau_h \frac{dh_i}{dt} = -h_i + h_\infty(c_i) \tag{13}$$

$$\tau_c \frac{dc_i}{dt} = -c_i + a_c \sum_{j\in S_i} \delta\left(t - t_j^i\right). \tag{14}$$

where $1/\tau_c$ is the rate at which calcium is cleared from the cell and $h_\infty(c)$ is a smooth sigmoidal activation curve of the form

$$h_\infty(c) = \frac{a_h}{\exp(-\beta(c-\gamma)) + 1} \tag{15}$$

Here β and γ are the gain and threshold of activation, respectively. Figure 2 illustrates the activation scheme for the linear synaptically activated AHP given by Eq. (12) (Fig. 2(a)) and the nonlinear calcium-mediated AHP given by Eqs. (13) and (14) (Fig. 2(b)).

2.2 Large-N limit: reduction to a mean-field description

2.2.1 Mean-field model for linear synaptic AHP

In order to derive a mean-field model, we first assume that the total input $u_i \equiv s - h_i + x_i + I_v$ in Eq. (1) is slowly varying relative to the fast membrane dynamics as specified by τ_v. For simplicity we set the threshold to unity ($\theta = 1$) and the reset level to negative unity ($v_r = -1$). Solving the LIF Eq. (1) for constant input u_i

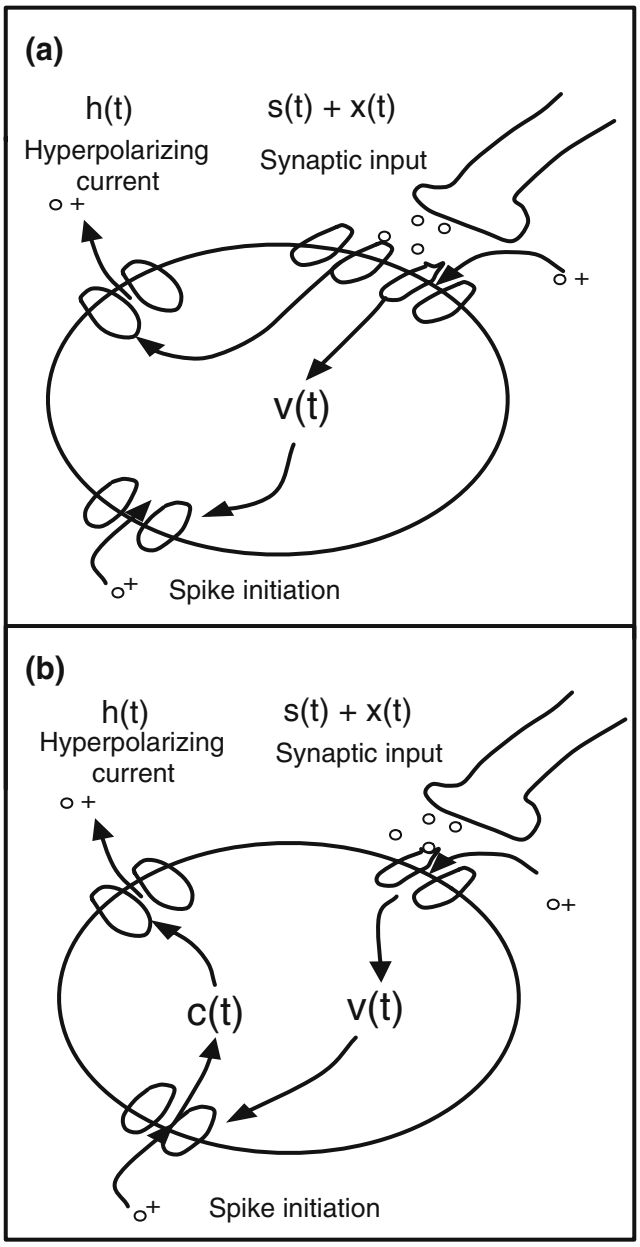

Fig. 2 Schematic diagram of the two different AHP models. (**a**) Linear synaptically activated AHP current evolving according to Eq. (12). (**b**) Non-linear calcium-mediated AHP current given by Eqs. (13) and (14)

shows that each neuron fires spikes at a uniform rate $f(u_i)$ with

$$f(u) = \frac{1}{\tau_r + \ln\left(\frac{u+1}{u-1}\right)}\Theta(u-1), \tag{16}$$

where Θ is the Heaviside step function. When u_i is time–dependent but slowly varying, we can still use $f(u_i)$ to represent the short-term average firing rate of the neuron. The assumption that synaptic inputs are slowly varying also means that we can perform a short-term time average of Eq. (3) and replace the input spike trains by a mean firing rate according to

$$\frac{1}{N}\sum_{i=1}^{N}\sum_{j\in S_i}\delta\left(t-t_j^i\right) \to \frac{1}{N}\sum_{i=1}^{N} f(u_i). \tag{17}$$

There are two factors that make this a reasonable approximation. First, there is the separation of time–scales $\tau_v \ll \tau_s, \tau_x$. Second, in the case of a sufficiently large network, population averaging contributes to smoothing out the synaptic input s, assuming that the neurons fire asynchronously. It follows that the approximation Eq. (17) will tend to break down at low spike rates and small N. Finally, the separation of time-scales ($\tau_h \gg \tau_s, \tau_x$) allows us to adiabatically eliminate $x_i(t)$ from Eq. (12) (see Gardiner 2004). That is, the slow variable h_i cannot effectively track the relatively fast fluctuations of $x_i(t)$ and we can replace x_i by its mean value $\langle x_i\rangle = 0$ in the h Eq. (12).

It follows from the above analysis that in the large–N limit, the population dynamics reduces to the set of mean field equations

$$\tau_h\frac{dh}{dt} = -h + a_h s \tag{18}$$

$$\tau_s\frac{ds}{dt} = -s + w \tag{19}$$

$$\tau_s\frac{dw}{dt} = -w + a_s\langle f\rangle. \tag{20}$$

where $\langle f\rangle$ represents the population (ensemble) average of the firing rates of each cell

$$\langle f\rangle = \lim_{N\to\infty}\frac{1}{N}\sum_{i=1}^{N} f(s-h_i+I_v+x_i)$$
$$= \int f(s-h+I_v+x)\,p(x)dx. \tag{21}$$

Here $p(x)$ is the steady–state Gaussian distribution for the Ornstein–Uhlenbeck noise process given by Eqs. (10) and (11):

$$p(x) = \sqrt{\frac{2}{\pi\sigma^2}}\mathrm{e}^{-\left(\frac{2x}{\sigma}\right)^2}. \tag{22}$$

Note that in the large–N limit we have used ergodicity to replace the sum over the N time–dependent random variables x_i by an integral over the stationary distribution $p(x)$. Hence, the ensemble averaged firing rate is shaped by noise through a convolution of f with a Gaussian distribution Eq. (22), where the noise strength σ controls the width of the Gaussian.

2.2.2 Mean-field reduction for nonlinear calcium-activated AHP

In the case of calcium-activated AHP, the h_i dynamics cannot so easily be adiabatically reduced because of the presence of nonlinearities. Carrying out time–averaging as in the previous example leads to the stochastic activation dynamics

$$\tau_h \frac{dh_i}{dt} = -h_i + h_\infty(c_i) \tag{23}$$

$$\tau_c \frac{dc_i}{dt} = -c_i + a_c f(s - h + I_v + x_i). \tag{24}$$

We see that stochastic fluctuations in the calcium concentration driven by synaptic noise can be amplified by the nonlinearities f and h_∞. Such an effect will be particularly strong when c_i is close to the activation threshold γ and the gain β is large, see equation Eq. (15). In order to carry out a mean–field reduction, we need to average these equations with respect to x_i under the approximations $\langle f(I + x_i)\rangle = f(\langle (I + x_i)\rangle)$ and $\langle h_\infty(c_i)\rangle = h(\langle c_i\rangle)$. Combining this with averaging the synaptic equations as in the previous case, we obtain the following mean-field model:

$$\tau_h \frac{dh}{dt} = -h + h_\infty(c) \tag{25}$$

$$\tau_c \frac{dc}{dt} = -c + f(s - h + I_v) \tag{26}$$

$$\tau_s \frac{ds}{dt} = -s + w \tag{27}$$

$$\tau_s \frac{dw}{dt} = -w + a_s \langle f \rangle. \tag{28}$$

In spite of the severe approximations involved in carrying out this reduction, we find numerically that the mean–field model captures well the dynamics of the full spiking model in the large-N limit (see Section 3). Note that the mean–field analysis of (Vladimirski et al. in press) handles nonlinearities in a similar fashion.

2.2.3 Stability analysis of the mean-field equations

We now have two different mean-field models, depending on the choice of linear activation Eq. (18) or nonlinear activation Eq. (25). In Section 3 we show that these two systems exhibit noise–induced burst oscillations via distinct bifurcation mechanisms. The starting point for the bifurcation analysis is to consider the stability of steady–state solutions. Recall from Eq. (16) that the firing rate function f is monotonic increasing, implying that $\langle f \rangle$ is also a monotonically increasing sigmoidal function of $s - h$. In the linearly activated case Eq. (12), solving for a steady state (h^*, s^*, w^*), where $h^* = a_h s^*$, allows a reduction to a single-variable fixed-point equation

$$0 = -s^* + \sqrt{\frac{2}{\pi\sigma^2}} \int f(z) e^{-2[\frac{z-((1-a_h)s^* + I_v)}{\sigma}]^2} dz. \tag{29}$$

The second term in Eq. (29) intersects the straight line $s = s^*$ to form one, two, or three steady state solutions, depending on the exact shape of f and σ. For notational simplicity we set $k_j = 1/\tau_j$, for $j = u, h, s$. We linearize Eqs. (18–20) about the fixed point by setting $z = z^* + \Delta z e^{\lambda t}$ for $z = (h^*, s^*, w^*)^T$ and expanding to first order in Δz. This generates the linearized system

$$\frac{d\Delta z}{dt} = \begin{pmatrix} -k_h & a_h k_h & 0 \\ 0 & -k_s & k_s \\ -k_s A & k_s A & -k_s \end{pmatrix} \Delta z, \tag{30}$$

where

$$A = \frac{4\sqrt{2}a_s}{\sigma^3\sqrt{\pi}} \int_{\mathbb{R}} x f(s - h + I_v + x) e^{-2\left(\frac{x}{\sigma}\right)^2} dx, \tag{31}$$

The real part of the eigenvalues of the linearized system Eq. (30) indicate the stability of the fixed point.

In the nonlinearly activated system Eq. (13) the method is much the same as above except the fixed point $z = (h^*, c^*, s^*, w^*)^T$ is defined by

$$h^* = h_\infty \circ f(s^* - h^* + I_v), \tag{32}$$

where $\circ$ represents functional composition, and

$$0 = -s^* + \sqrt{\frac{2}{\pi\sigma^2}} \int f(z) e^{-2[\frac{z-(s^* - h^* + I_v)}{\sigma}]^2} dz, \tag{33}$$

and the linearized equation for Δz is

$$\frac{d\Delta z}{dt} = \begin{pmatrix} -k_h & k_h h'_\infty & 0 & 0 \\ -k_c f' & -k_c & k_c f' & 0 \\ 0 & 0 & -k_s & k_s \\ -k_s A & 0 & k_s A & -k_s \end{pmatrix} \Delta z, \tag{34}$$

where the prime indicates derivative in the input variable evaluated at the fixed point z.

2.3 Numerical methods for the spiking model

Numerical simulations are implemented using the MATLAB (Mathworks inc.) computing environment with a simple forward Euler variable time step algorithm for the h_i, s, w, x_i, and y_i variables, where the y_i are integrated stochastically (see Gardiner 2004). For simplicity we set the threshold to unity ($\theta = 1$) and the reset level to negative unity ($v_r = -1$). We also choose $\tau_v = 1$ms as a baseline time scale for the model. To

correctly model the refractory period, upon spiking, we reset v_i to $v_r - 1$ and define the v_i dynamics to be

$$\frac{dv_i}{dt} = \frac{1}{\tau_r}, \quad v_i < v_r. \tag{35}$$

Hence, upon spiking v_i will increase linearly to v_r in time τ_r. Let $u_i^j = s - h_i^j + x_i^j + I_v$ denote the total input to the ith cell at the jth discrete time step and let v_i^j denote the corresponding membrane potential. We treat u_i^j as constant on a short time scale and calculate analytically the time to spike $\mathcal{T}_i^j$ for each v_i^j according to

$$\mathcal{T}_i^j = \begin{cases} \ln\left(\frac{-v_i^j + I_v + u_i^j}{u_i^j + I_v - 1}\right), & u_i^j + I_v > 1 \\ \infty, & \text{otherwise} \end{cases} \tag{36}$$

We choose an upper and a lower bound on time steps Δt_{min} and Δt_{max}. For the j^{th} iteration of the algorithm a time step Δt_j is chosen by minimizing the following set

$$\Delta t_j = \min\left\{\Delta t_{max}, \left\{\{\mathcal{T}_i^j\}_{i=1}^N | \mathcal{T}_i^j > \Delta t_{min}\right\}, \right\}, \tag{37}$$

where the maximum time step is chosen small enough to ensure sufficient accuracy of the input variables, and the minimum time step is chosen to provide sufficient temporal fidelity of spike times. Those $\mathcal{T}_i^j$ that are smaller than Δt_j will fire during the time step and their somatic voltages are advanced to $v_i^{j+1} = v_r - 1 + (\Delta t_j - \mathcal{T}_i^j)/\tau_r$ for the next time step. For those that do not fire but are above v_r (they are "online") the voltage is advanced by the analytical solution of the LIF equation,

$$v_i^{j+1} = e^{-\Delta t_j} v_i^j + \left(1 - e^{-\Delta t_j}\right)\left(u_i^j + I_v\right) \tag{38}$$

Those v_i^j that are below $v_r - \Delta t_j/\tau_r$, so that they are offline and stay offline during the time step Δt_j, are advanced to $v_i^{j+1} = v_i^j + \Delta t_j/\tau_r$. Finally, those v_i^j that will come online during the interval Δt_j ($v_i^j > v_r - \Delta t_j/\tau_r$) are then advanced to

$$v_i^{j+1} = e^{-z} v_r + (1 - e^{-z})\left(u_i^j + I_v\right), \tag{39}$$

where $z = \Delta t_j - \tau_r(v_r - v_i^j)$. Upon each time step, the number of spikes k that occur during Δt_j is then fed into the synaptic integrator

$$w^{j+1} = -\frac{w^j}{\tau_s} + \frac{a_s}{\tau_s} k. \tag{40}$$

This algorithm accurately keeps track of spike times and offline-to-online transitions assuming the u_i are constant over each short time step. The algorithm is based on Shelly and Tao (2001) second-order numerical scheme of integrate–and–fire cells, which approximates the synaptic response times as in Eq. (40) (while still guaranteeing second-order convergence). However, we have replaced their second-order Runge-Kutta time step and backward linearly interpolated spike time estimate with the analytical solution Eqs. (38–39) because in our model the inputs change slowly.

3 Results

3.1 Linear synaptically activated AHP

Numerically solving the large-N LIF spiking network given by Eqs. (1–3), Eqs. (10) and (11) with linear synaptically activated AHP currents, Eq. (12), establishes that for an appropriate choice of parameters the network can produce regular spontaneous burst oscillations. Figure 3 illustrates these synchronized population bursts for a network of $N = 500$ neurons. The top panel (Fig. 3(a)) shows the network synaptic activity $s(t)$ for the stochastic spiking model (solid line) and the mean-field model (dashed line) for $N = 500$ cells. Figure 3(b)

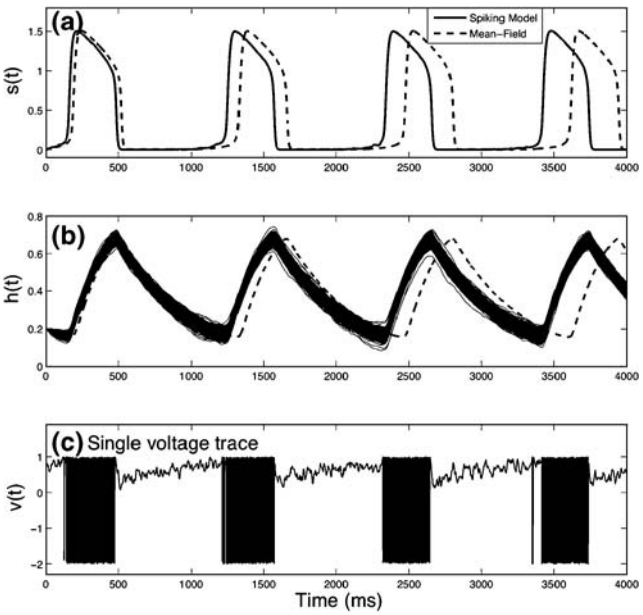

Fig. 3 Stochastic simulations of the spiking network model for $N = 500$ and a linear synaptically activated AHP current, Eqs. (1–3), (10), (11) and (12). Corresponding mean field solution of Eqs. (18–20) is shown by *dashed curves*. (**a**) $s(t)$ trace, (**b**) $h_i(t)$, $i = 1 \ldots N$ traces are depicted as *thin solid lines*; mean-field h depicted by a *gray dashed line*. (**c**) shows a single voltage trace of the stochastic spiking model. The neuron spikes upon reaching threshold ($\theta = 1$) and is reset to -2 and held offline for a refractory time τ_r during which it increases to v_r and is put back online. Notice the stochastic voltage fluctuations between bursts and the variable burst duration at the single-cell level, in addition to the random smaller spiking events in between the main bursts. The parameters are $\tau_v = 1$ms, $\tau_h = 500$ms, $\tau_s = 5$ms, $\tau_x = 5$ms, $I_v = 0.95$mv, $\sigma = 0.25$, $v_r = -1$, $\theta = 1$, $\tau_r = 1$ms, $a_s = 3$, and $a_h = 1$

shows all the $h_i(t)$ variables as thin solid lines clustered tightly together throughout every oscillation cycle. The mean-field $h(t)$ is indicated by the grey dashed line. The mean-field model matches well with the large-N spiking model, although the oscillation period is roughly 3-6% longer than the stochastic simulations. Note that the $h_i(t)$ variables have a small variation over a burst cycle indicating that the adiabatic elimination is a reasonable approximation. The population-level synaptic variable $s(t)$ is also very smooth. Examination of a single voltage trace (Fig. 3(c)) indicates that at the single cell level the burst duration is variable and smaller spiking episodes randomly occur in the inter-burst cycle. To illustrate the randomness of the single–cell spiking behavior, we show a single burst cycle in a raster plot for 20 cells from the $N = 500$ in Fig. 4. The network spiking initially climbs slowly during a kindling stage due to the slow decay of the AHP current. Once the spiking is high enough, the network accelerates quickly through positive synaptic feedback to a high rate of spiking (the burst) which then terminates to a quiescent state through the activation of the AHP. The decay of AHP triggers a subsequent kindling stage, thus forming an oscillation. Notice that in the pre-burst kindling stage multiple spike events occur in quick succession due to the slowly fluctuating noise.

The population burst oscillation can be controlled by noise. Figure 5 plots the synaptic $s(t)$ variable of the large-N spiking model (solid line) and the mean-field reduction (dashed line) over nearly two orders of magnitude of noise levels from $\sigma = 0.025$ to $\sigma = 0.95$.

For the particular choices of model parameters we observe that for very low noise levels (Fig. 5(a); $\sigma = 0.025$) no burst oscillations are observed. As noise is increased, burst oscillations are seen to emerge in both the spiking model and the mean-field model. Figure 5(b) shows that there is a discrepancy between the precise onset of existence of the burst oscillations between the two models. Both Figs. 3 and 5 suggest that the mean-field model is slightly less active and underestimates the burst frequency of the spiking model. As the noise level is increased to large noise levels, both models increase their burst frequency and their amplitudes diminish. At sufficiently high noise levels neither the mean-field model nor the spiking model support burst oscillations. Figure 6 summarizes the relationship between noise and burst frequency for the

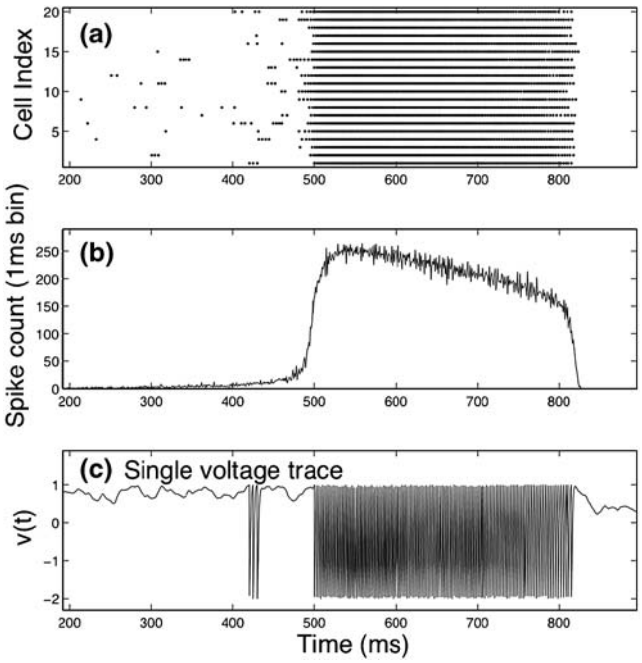

Fig. 4 Stochastic simulation of the network model with linear AHP given by Eqs. (1–3), (10) (11) and (12) for $N = 500$ and $\sigma = 0.25$. (**a**) Raster plot of 20 of the 500 cells. Individual spike times (abscissa) are indicated by a *single black dot* for the $i = 1 \ldots 20$ cells (ordinate). (**b**) Spike counts for the $N = 500$ network in 1 ms bins revealing that the network is asynchronously activated on a 1 ms time scale. (**c**) Single voltage trace $v(t)$ of the $i = 1$ cell. Notice the small spiking events that occur preceding prior to the main population burst. All other parameters are the same as in Fig. 3

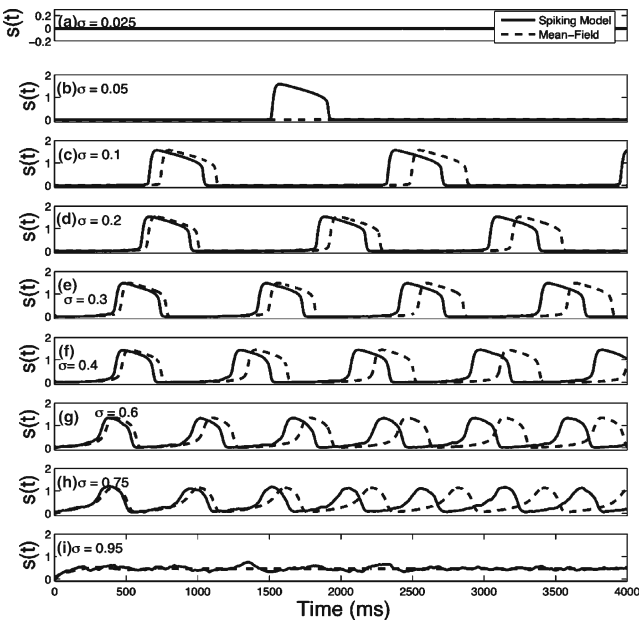

Fig. 5 Control of oscillations by noise for linear AHP model. The population synaptic input $s(t)$ for the stochastic spiking model (*solid line*) and the mean-field model (*dashed line*) over nine noise strength levels spanning two orders of magnitude ((**a**) to (**i**)). At low noise ($\sigma = 0.025$; (**a**)) no oscillations are observed. As noise is increased, burst oscillations emerge and increase in frequency. At high noise the frequency speeds up and the amplitude is squashed. The mean-field model matches well with the qualitative behavior of the spiking model. All other parameters are the same as in Fig. 3

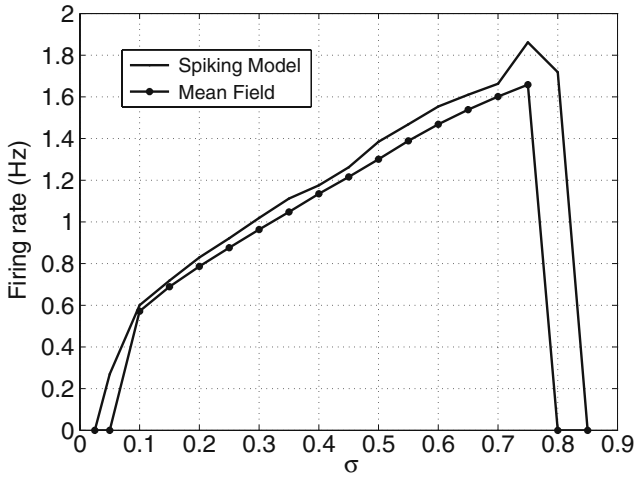

Fig. 6 The population burst frequency for the stochastic spiking model with linear AHP (*solid line*) and the corresponding mean-field model (*ball-linked line*) over 18 noise strength levels spanning two orders of magnitude from $\sigma = 0.025$ to $\sigma = 0.85$. There exists a window of noise levels that support oscillations. Within that window frequency increases with increasing noise. The mean-field model predicts well the behavior of the spiking model, with a 3–6% frequency difference. All other parameters are the same as in Fig. 3

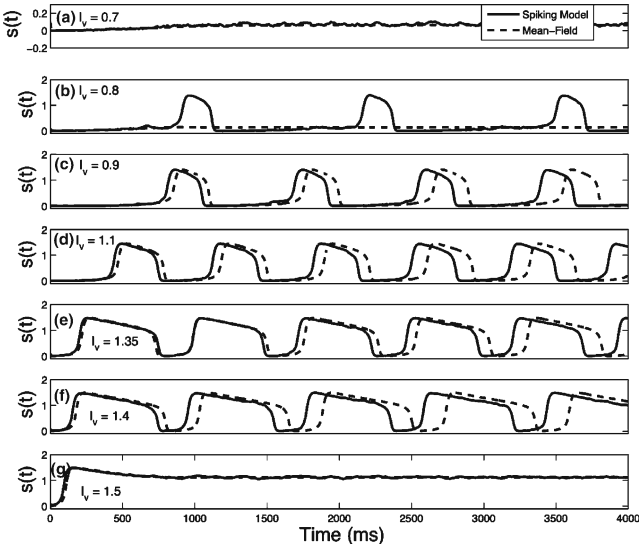

Fig. 7 Varying bias current in linear AHP model. The population synaptic input $s(t)$ for the stochastic spiking model (*solid line*) and the mean-field model (*dashed line*) over seven bias current levels ((**a**) to (**g**)) for a fixed noise level $\sigma = 0.45$. For sufficiently low noise no oscillations are observed. As current is increased, burst oscillations emerge and increase in frequency. At sufficiently high current the oscillations disappear but with no accompanying amplitude modulation, unlike Fig. 5 where we varied noise strength. The mean-field model matches well with the qualitative behavior of the spiking model. All other parameters are the same as in Fig. 3

spiking model and mean-field model over a similar range of noise levels as shown in Fig. 5.

Burst oscillations can also be controlled by the applied bias current I_v. Figure 7 shows the variation of I_v for a fixed $\sigma = 0.45$.

At low current levels no oscillations are observed and the network is in a low activity steady state (Fig. 7(a)). Increased bias current produces oscillations, and the burst oscillation frequency increases with increased current (Figs. 7(b-f)). At sufficiently high current levels the system oscillations disappear and the network is now in a high activity steady state (Fig. 7(g)).

We find that the presence of noise can increase the available frequency range of burst oscillations of the system as I_v is varied. Figure 8 shows the firing rate (Hz), indicated by grayscale in (Fig. 8(a)), as a function of both the bias current I_v (abscissa) and noise σ (ordinate).

For this figure the shaded patch associated with a certain firing rate corresponds to the parameter pair associated with the lower left vertex of each grid square. For low noise levels ($\sigma = 0.025$) a sweep through increasing bias currents can achieve a limited range of firing rates, from approximately 0.5 to 0.75 Hz, as shown by the solid dotted black line in Fig. 8(a) and (b). However, linearly increasing the noise with the bias current as in the case of Poisson background inputs, see section 2.1.1, can produce firing rates in a much wider range. This is indicated by the open circled line in Fig. 8(a) and (b), which shows the frequency varying from approximately 0.5 to 2.5 Hz, corresponding to an eight fold increase in available frequencies compared to varying current alone with very low noise. Thus, the inclusion of noise in the system increases the robustness of the oscillation.

The slight overestimation of the period by the mean-field model shown in Figs. 3 and 5 was observed for any parameter choices that elicited burst oscillations. The discrepancies between the mean-field model and the large-N spiking model are due to a number of factors that are neglected in the derivation of the mean-field model. (a) Fluctuations in the slow activation variable $h_i(t)$ driven by the synaptic noise $x_i(t)$, see Eq. (12). (b) As mentioned earlier, at low firing rates a scalar firing rate description of spike activity breaks down because temporal averaging of spike emission must be carried out over long time scales. At higher firing rates this will not be a problem. This is supported by the observation the mean-field model captures very well the shape of the spike model burst at high firing rates, but not as well at low rates. (c) For finite N, the population average $\langle f \rangle$ of Eq. (21) randomly fluctuates about the ensemble average over the stationary distribution $p(x)$. Reduction of network size produces irregular burst amplitudes and periods (data not shown). All of the preceding factors introduce discrepancies between the mean-field equations and the spiking model. The value

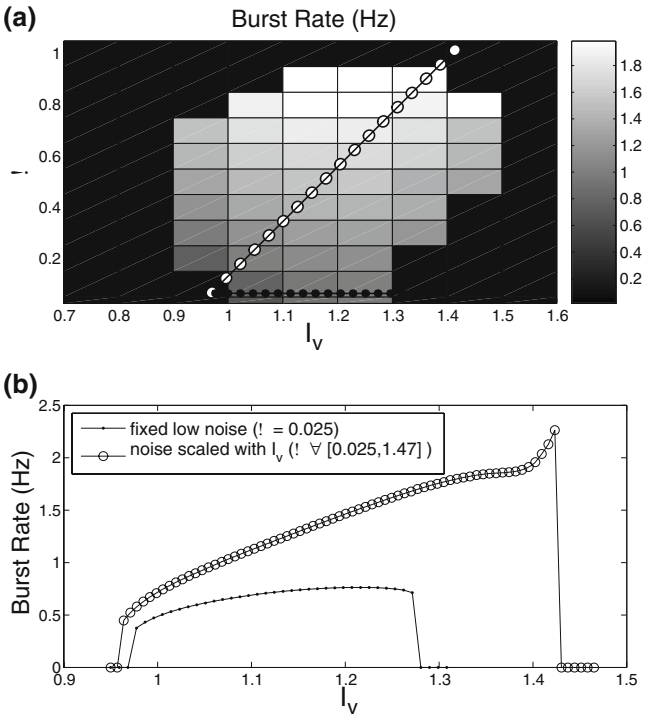

Fig. 8 (**a**) The population burst frequency for the mean-field model with linear AHP, indicated by greyscale (*right*) as a function of the bias current I_v (abscissa) and noise σ (ordinate). (**b**) Fine grained burst rate as a function of I_v (*solid dotted line*) with $\sigma = 0.025$ (*black dot path* in (**a**)), and as a function of both I_v and σ scaled together: $\sigma(I_v) = 0.025 + (1.47 - 0.025)(I_v - 0.95)/(1.47 - 0.95)$ (*open circled dotted line*; path shown in (**a**)). All other parameters are the same as in Fig. 3

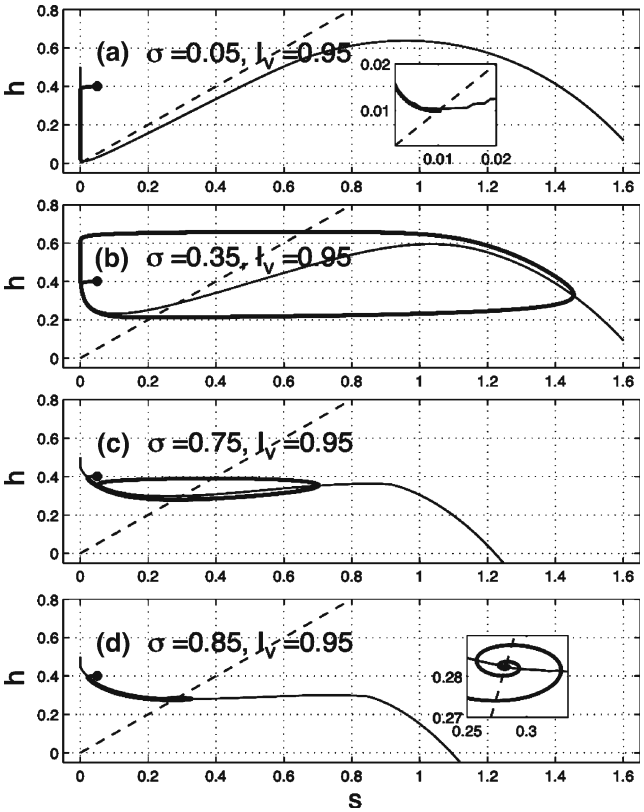

Fig. 9 Varying noise in the phase plane for linear AHP model. Projected mean-field dynamics in the *s*–*h* plane for four noise levels (**a**–**d**) and fixed bias current $I_v = 0.95$. The mean-field solution (*thick solid line*) evolves from an initial condition marked by a *dot* ($\cdot$). For low noise ((**a**), $\sigma = 0.05$) the system settles into a low-activity fixed point indicated by the intersection of the projected null surfaces (see *inset*) of *s* and *h* (*thin solid line* and *thin dashed line*, respectively). With increased noise ((**b**), $\sigma = 0.35$) a large amplitude oscillation emerges. At $\sigma = 0.75$ ((**c**)) the oscillation amplitude diminishes. (**d**) At high noise $\sigma = 0.95$ there exists a stable spiral. The same parameters are used as in Fig. 3

of deriving the mean-field equations, however, does not lie in reproducing the spiking model precisely, but in permitting mathematical analysis of the dynamical mechanisms that produce bursting.

We now focus on the bifurcation structure of the mean–field Eqs. (18–20). We proceed by projecting the solution of these equations onto a two-dimensional submanifold along with the projected null surfaces to gain insight into the system behavior. Figure 9 shows the projected solution (thick solid line) in the *s*-*h* phase plane along side the projected *s* null surface (thin solid line) and *h* null surface (thin dashed line) for four noise levels (Fig. 9(a–d)). For low noise levels the system settles onto a stable fixed point representing a "silent" or low activity state; the inset in Fig. 9(a) suggests that the stability of the fixed point is stable. Panel (b) of Fig. 9 reveals that large enough noise can produce deterministic oscillations. Geometrically, the oscillation emerges as the leftmost local minimum of the projected *s* null surface elevates with respect to the fixed *h* null surface. As the intersection of the surfaces moves rightward with increasing σ, it appears to become unstable. By numerically calculating the eigenvalues of the linearized system about this fixed point as in Eq. (30), we find that the real part of a single complex eigenvalue pair goes from negative to positive if noise is elevated above a certain threshold. The first Lyapunov coefficient (see Kuznetsov 2004) at this bifurcation point is positive. Hence, the fixed point destabilizes in a subcritical Hopf bifurcation. An analogous mechanism of rhythmogenesis occurs in two-variable models of single-cell excitable membranes such as the Fitzhugh-Nagumo equations and the Morris-Lecar equations, both of which are examples of relaxation oscillators (Izhikevich 2007). Hence, during noise–induced population-level rhythmic bursting the globally coupled excitatory network acts like a low-dimensional relaxation oscillator. As the noise level is further increased the system undergoes a super-critical Hopf bifurcation at $\sigma = 0.95$, beyond which the network settles into a stable spiral (see inset of Fig. 9(d)).

Next we probe the mean-field system in the projected phase plane as we vary I_v and keep the noise fixed at an intermediate noise level. As suggested by Fig. 7, we find that the oscillation exists over a finite range of bias currents. Figure 10 shows the projected s–h phase plane over four bias currents. For low bias current (Fig. 10(a)) the system settles into a low-activity fixed point indicated by the intersection of the projected null surfaces (see inset) of s and h (thin solid line and thin dashed line, respectively). With increased current (Fig. 10(b)) a finite amplitude oscillation emerges that persists over a range of values of I_v without a significant change in amplitude (Fig. 10(c)). At sufficiently high bias currents (Fig. 10(d)) there exists a high-activity stable fixed point analogous to the low-activity resting state at low currents. Stability analysis of the fixed point over this parameter range shows that initiation and termination of bursting both occur via a subcritical Hopf bifurcation. Figure 11 illustrates the bifurcation results from Figs. 8, 9, and 10 in the I_v-σ parameter plane. The lower left corner, when noise and current are low, corresponds to the low-activity, non oscillatory "resting" state. Increasing noise or current can produce burst oscillations via a subcritical Hopf bifurcation where the state of the system enters the inner region encircled by Hopf bifurcation manifolds. Along the manifolds there are two codimension two Bautin bifurcation points separating supercritical Hopf (dashed line) and subcritical Hopf (solid line) boundaries. Moving to the right in this parameter space puts the system in a non oscillatory "high" activity state. The thin dotted lines represent the paths in parameter space that have been explored in the above analysis contained in Figs. 5, 8, and 7 corresponding to the vertical, diagonal, and horizontal dotted lines, respectively.

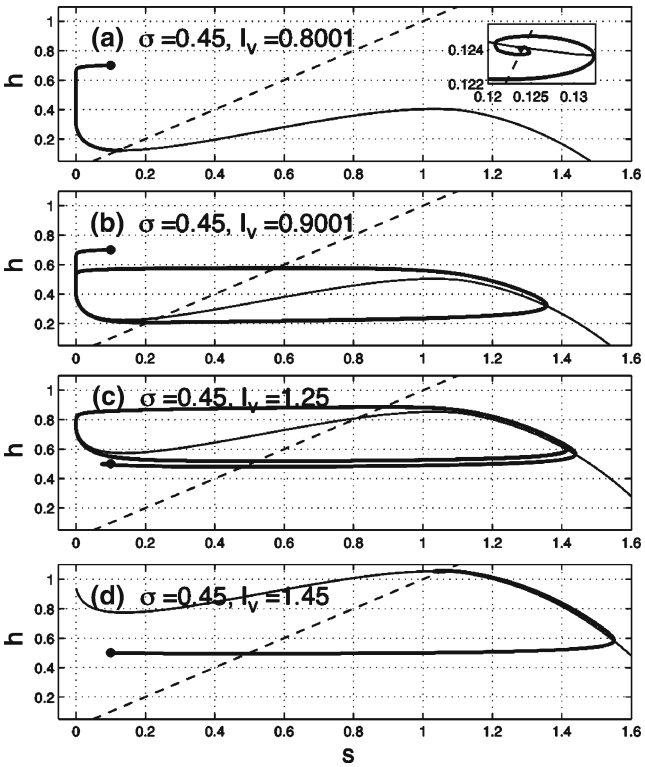

Fig. 10 Varying current in the phase plane for linear AHP model. Projected mean-field dynamics in the s–h plane for four bias current levels (**a**–**d**) and fixed noise $\sigma = 0.45$. The mean-field solution (*thick solid line*) evolves from an initial condition marked by a *dot* (·). For low bias current ((**a**), $I_v = 0.8$) the system settles into a low-activity fixed point indicated by the intersection of the projected null surfaces (see *inset*) of s and h (*thin solid line* and *thin dashed line*, respectively). With increased current ((**b**), $I_v = 0.9$) a large amplitude oscillation emerges. At $I_v = 1.25$ (**c**) the oscillation amplitude in s does not change much. (**d**) At high current $I_v = 1.45$ there exists a high-activity stable fixed point analogous to the low-activity state for low current. All other parameters are as in Fig. 3

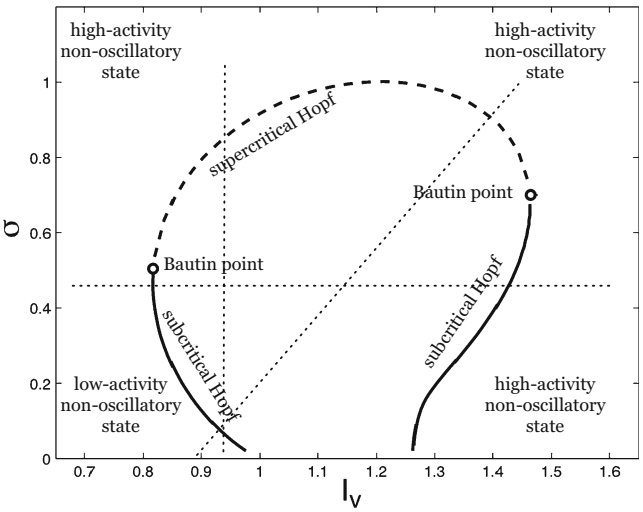

Fig. 11 Bifurcation diagram in I_v (abscissa) and noise σ (ordinate) with all other parameters as in Fig. 3. Burst oscillations exist in the interior of the region bounded by subcritical (*solid lines*) and supercritical Hopf curves (*dashed lines*), which meet at Bautin codimension-two bifurcation points (*open circles*). The *dotted lines* represent some of the paths in parameter space that have been explored in the above analysis, see Figs. 5, 8, and 7, correspond to the *vertical*, *diagonal*, and *horizontal dotted lines*, respectively

3.2 Nonlinearly activated AHP results

Numerical simulations of the spiking model Eqs. (1–3) with nonlinear activation of h (Eqs. (13) and (14)) establishes that oscillations exist for an appropriate set of parameters as shown in Fig. 12. As before, the mean-field model matches well the burst shape and period (Fig. 12(a)). Figure 12(b) shows all of the AHP

variables $h(t)$ (thin solid lines) and a single $c_1(t)$ trace of the spiking model (solid line), where the jagged $c_1(t)$ is due to a_c/τ_c discrete jumps upward corresponding to influx due to spike events from the cell in question. The mean field approximation (dashed lines) matches well, but for the $c(t)$ variable it only captures mean-value-like behavior because spikes are not explicitly modeled in the mean-field model. Just as in the linearly activating AHP model the single voltage spiking traces (Fig. 12(c)) reveal small spiking events in the run up to the large bursting events. Note that due to the nonlinear activation the variance of the $h_i(t)$ traces varies through the burst cycle, where during the silent state the AHP traces coalesce, and during the burst the traces disperse maximally at the peak of bursting. As we shall see, the mean-field approximation breaks down if the dispersion of the AHP traces is too great.

Just as with the linear AHP model, the modulation of noise strength of the nonlinear model can control the existence and period of the burst oscillations. Figure 13 reveals that at low noise levels burst oscillation existence and period can be predicted by the mean-field model Eqs. (25–28). At high noise levels, however, there is a significant mismatch between the two models (Fig. 13(f)). Discrepancies also arise between the models at high current levels. As can be seen in Fig. 12(b), the AHP traces disperse during the transition to and from bursting and coalesce during the silent phase. At high noise or current levels, the cells switch between these two states more often such that dispersion dominates cohesion of the AHP variables and the mean-field description breaks down. To illustrate this breakdown we simulate the nonlinear AHP spiking model and the mean-field reduction for two bias currents and a fixed noise value $\sigma = 0.25$, see Fig. 14. In these simulations (and all other simulations in this paper) we initialize the AHP variables to the same value (no dispersion). Over time the AHP variables will disperse as the random spiking of each cell differentially activates the respective AHP currents. Figure 14 panels (a) and (b) show the system with a lower level of bias current ($I_v = 1.80$) where the mean-field model matches very well the full spiking system. Changing the current to a larger amount ($I_v = 1.87$) causes the solution of the full spiking model to follow the mean-field model for one burst cycle, but on the second cycle, after the AHP traces have dispersed, the full spiking model diverges

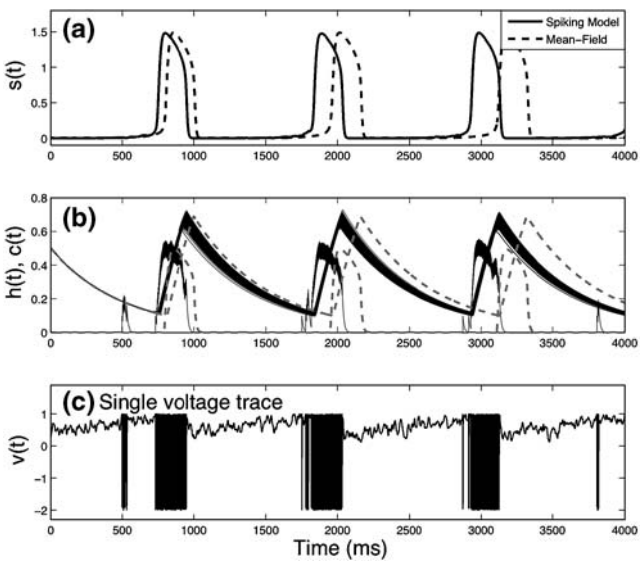

Fig. 12 Stochastic simulations of spiking network model for $N = 500$ and a nonlinear calcium activated AHP current, Eqs. (1–3), (10), (11), (13) and (14). Corresponding mean–field solution of Eqs. (18–20) is shown by *dashed lines*. (**a**) $s(t)$ trace, (**b**) All the $h_i(t)$ traces and a single $c_1(t)$ trace of the spiking model (*solid line*) are depicted along side the mean-field solutions $h(t)$ and $c(t)$ of Eqs. (13) and (14), which are depicted by *thick gray dashed lines*. (**c**) shows a single voltage trace of the stochastic spiking model. The neuron spikes upon reaching threshold ($\theta = 1$) and is reset to -2 and held offline for a refractory time τ_r during which it increases to v_r and is put back online. Notice the stochastic voltage fluctuations between bursts and the variable burst duration at the single-cell level, in addition to the random smaller spiking events in between the main bursts. The parameters are $\tau_v = 1$ ms, $\tau_h = 500$ ms, $\tau_s = 5$ ms, $\tau_x = 5$ ms, $\tau_c = 10$ ms, $I_v = 0.95$ mv, $\sigma = 0.2$, $v_r = -1$, $\theta = 1$, $\tau_r = 1$ ms, $a_s = 3$, $a_h = 2$, $a_c = 1$, and $\gamma = 0.3$, and $\beta = 100$

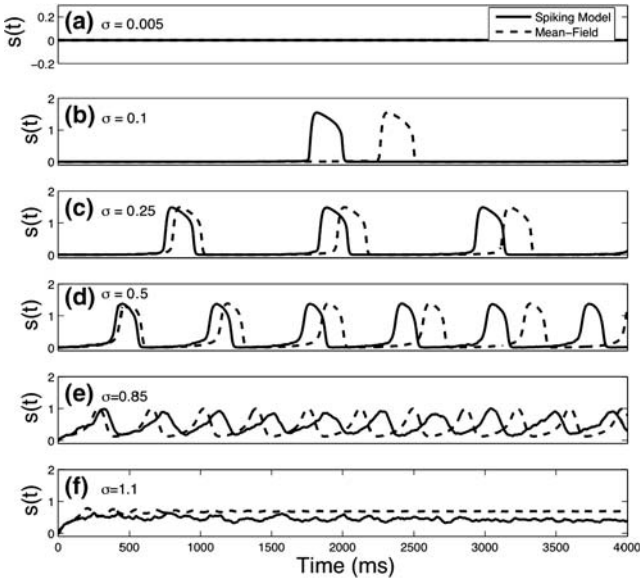

Fig. 13 Varying noise strength for nonlinear AHP model. The population synaptic input $s(t)$ for the stochastic spiking model (*solid line*) and the mean-field model (*dashed line*) over six noise strength levels spanning two orders of magnitude ((**a**) to (**f**)). At low noise ($\sigma = 0.025$; (**a**)) no oscillations are observed. As noise is increased, burst oscillations emerge and increase in frequency. At high noise the frequency speeds up and the amplitude is squashed. The mean-field model matches well with the qualitative behavior of the spiking model except at the highest noise level (**f**). All other parameters are the same as in Fig. 12

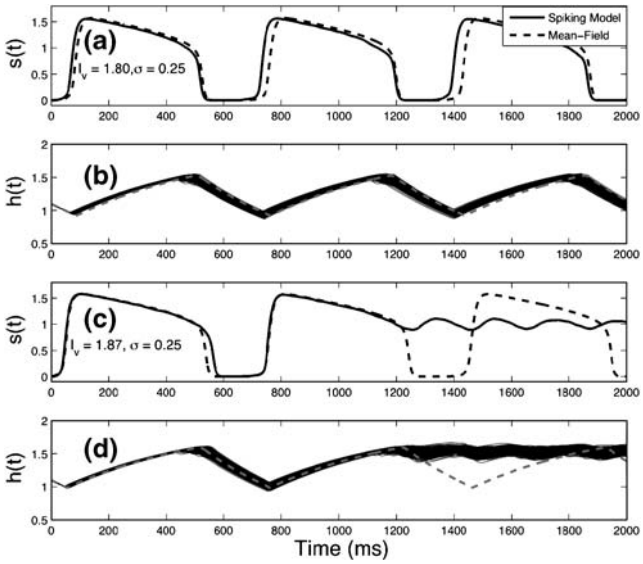

Fig. 14 Breakdown of mean-field theory in nonlinear AHP model. The population activity at two high current levels $I_v = 1.8$ ((**a**) and (**b**)) and $I_v = 1.87$ ((**c**) and (**d**)) illustrate how the mean-field model breaks down when AHP dispersion is too great. (**a**) and (**c**) show synaptic input $s(t)$ for the stochastic spiking model (*solid line*) and the mean-field model (*dashed line*). (**b**) and (**d**) show all the $h_i(t)$ variables (*thin black lines*) and the mean-field $h(t)$ variable (*thick grey dashed line*). All other parameters are the same as in Fig. 12

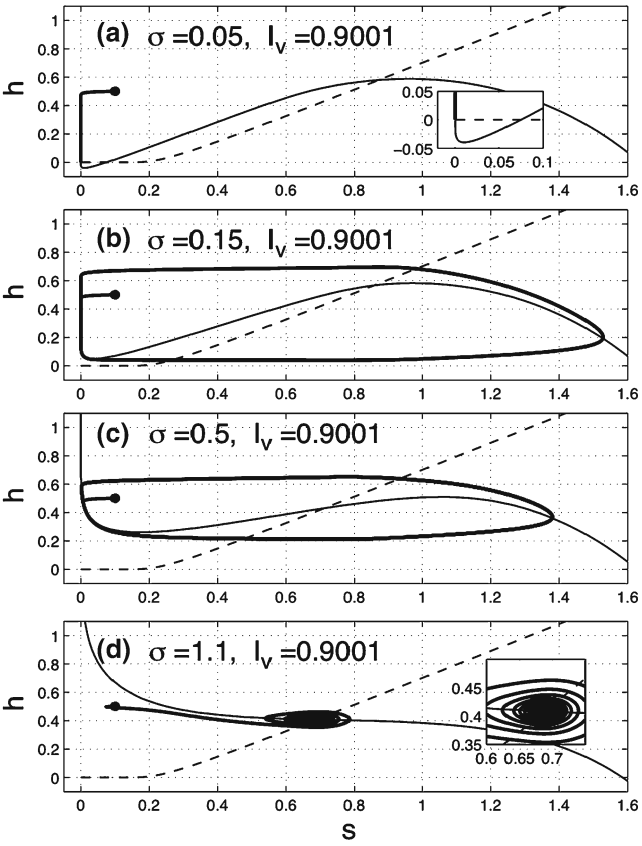

Fig. 15 Increasing noise produces a SNIC in nonlinear AHP model. Projected mean-field dynamics Eqs. (18–20) of the nonlinear calcium mediated AHP in the *s*-*h* plane for four noise levels (**a**–**d**) and fixed bias current $I_v = 0.9001$. The mean-field solution (*thick solid line*) evolves from an initial condition marked by a dot (·). For low noise ((**a**), $\sigma = 0.05$) the system settles into a low-activity fixed point indicated by the leftmost intersection of the projected null surfaces (see *inset*) of *s* and *h* (*thin solid line* and *thin dashed line*, respectively). With increased noise ((**b**), $\sigma = 0.15$) a large amplitude oscillation emerges. At $\sigma = 0.5$ (**c**) the oscillation amplitude diminishes. (**d**) At high noise $\sigma = 1.10$ (where the mean-field system is no longer a valid predictor of the full spiking model) there exists a stable spiral (see *inset*). The same parameters are used as in Fig. 12

from the mean-field prediction. Because of this effect, we restrict our subsequent analysis of the non-linear AHP mean-field system to low noise and bias current levels, where the mean-field model is quantitatively predictive.

By carrying out phase plane and bifurcation analysis of the calcium mediated AHP mean-field Eqs. (18–20) we will establish that the noise-induced mechanism of burst rhythm onset is due to a SNIC bifurcation. First we note that the projected *s* null surface for both the linear and nonlinear models are identical, being given by Eq. (33). On the other hand, the projected null surface of the *h* variable is now nonlinear, see Eq. (32). Figure 15 shows the evolution of the mean-field system in the *s*-*h* projected plane for four increasing noise levels (panels (a–d)). At low noise levels the null surfaces intersect to form three fixed points (Fig. 15(a)). The rightmost fixed point is unstable. The leftmost fixed point, which is stable (see inset of Fig. 15(a)), and the middle fixed point, which is unstable are formed by the local minimum of the *s* null-surface crossing with the horizontal "foot" of the *h* null-surface. As the noise level is increased, the local minimum of the projected *s* null-surface elevates with respect to the foot of the *h* null-surface, causing the left and middle fixed points to disappear in a saddle node bifurcation, leaving a periodic solution in its place (Fig. 15(b)). As the noise is increased further the slope of the middle section of the *s* null surface becomes less positive and the amplitude of the oscillation as measured in the *h* or the *s* dimension is decreased (Fig. 15(c)). At very high noise levels the mean-field system undergoes a supercritical Hopf bifurcation to a non-oscillatory state (Fig. 15(d)). Numerical simulations of the full spiking model suggest a similar qualitative behavior in the high-noise regime (data not shown), but the mean-field model can make no quantitative predictions here.

Finally, increasing the bias current can also give rise to a SNIC bifurcation to burst oscillations in the nonlinear calcium-mediated AHP model. Figure 16 shows the evolution of the mean-field system in the *s*-*h* projected plane for two current levels (panels (a) and (b)). In a

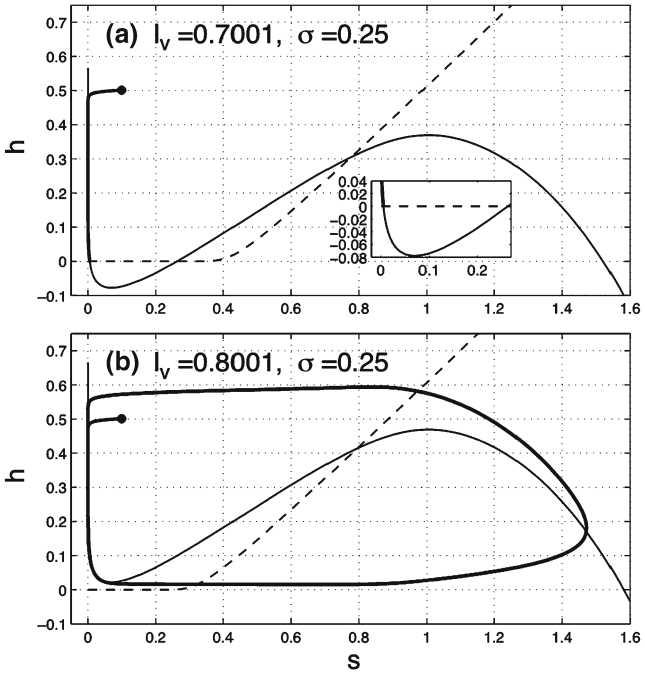

Fig. 16 Increasing current produces a SNIC in nonlinear AHP model. Projected mean-field dynamics Eqs. (18–20) of the nonlinear calcium mediated AHP model in the *s*-*h* plane for two current levels ((**a**) and (**b**)) and fixed noise $\sigma = 0.25$. The mean-field solution (*thick solid line*) evolves from an initial condition marked by a *dot* ($\cdot$). For low current ((**a**), $I_v = 0.7$) the system settles into a low-activity fixed point indicated by the leftmost intersection of the projected null surfaces (see *inset*) of *s* and *h* (*thin solid line* and *thin dashed line*, respectively). With increased current ((**b**), $I_v = 0.8$) a large amplitude oscillation emerges. The same parameters are used as in Fig. 12

similar fashion to increasing the noise at fixed bias current, the nonlinear AHP mean-field model undergoes a SNIC through flattening of the projected *s* null-surface, where upon the leftmost two fixed point intersections shown in Fig. 16(a) collide and annihilate leaving a periodic solution shown in Fig. 16(b).

4 Discussion

In this paper we have shown that a globally connected excitatory network of LIF model neurons possessing a slow activity-dependent adaptation current can exhibit coherent population burst oscillations when driven by synaptically filtered noise. Due to the time scale separation imposed by the slow AHP current and synaptic filtering ($\tau_v \ll \tau_x, \tau_s \ll \tau_h$) we were able to derive low-dimensional deterministic mean-field equations for the two different AHP currents in the large-N limit. The mean-field dynamical systems are amenable to mathematical analysis and we have shown that noise induced bursting can come about through a subcritical Hopf bifurcation in the linear synaptically activated AHP model, and a SNIC bifurcation in the nonlinear calcium-mediated model. In the linear model, by analyzing the joint dependence of the oscillations on the noise strength σ and the overall excitability (as determined by the bias current I_v), the burst oscillations are predicted to exist within an "island" of the I_v-σ parameter space determined by a continuous Hopf bifurcation curve (Fig. 11). Moreover, by conceiving the noise source as a Poisson input we reason that an increase in input strength a_x or the Poisson rate ν will scale both the noise and bias current together, suggesting a natural diagonal (rightward increasing) pathway through I_v-σ parameter space. We have shown that for a particular choice of parameters that this pathway through I_v-σ space can afford both a larger parameter range that supports oscillations and a frequency range that is many times greater (approximately eight times) compared to the zero noise case.

Our results complement the work of Van Vreeswijk and Hansel (2001), who have studied the basic principles of emergent population burst oscillations in deterministic networks, and Vladimirski et al. (in press), who have shown through mean-field analysis that population heterogeneity can provide added robustness to population burst oscillations. Furthermore, the present work is distinct from other studies on noise–induced population burst oscillations, including both mean–field models at fixed noise levels (Gigante et al. 2007) (Vladimirski et al. in press), and conductance–based models of intrinsically activated currents (Kosmidis et al. 2004).

The derivation of the mean-field model rests on several approximating assumptions, including the aforementioned separation of time scales, and the asynchrony of spiking in the large-N network. We also assume the ergodicity of the large-N system so as to use the steady state Gaussian probability density $p(x)$, Eq. (22), in order to integrate the firing rate function over the random inputs as in Eq. (21). We have shown that the nonlinear calcium-mediated AHP mean-field model is only valid for sufficiently small currents or noise levels where the $h_i(t)$ variables are not dispersed too much. At higher current and noise levels, oscillatory behavior can still persist, but the full spiking model behavior cannot be predicted by the mean-field system. More generally, we note that the requirements for the validity of the mean-field model are not necessary conditions for oscillatory behavior in the full spiking model. In fact, we have observed that direct input of white noise to the membrane equation in lieu of synaptic filtering Eqs. (10), (11) can also produce robust population oscillations. We leave the systematic study of fast noise inputs for future work.

As stated in the introduction, Kosmidis et al. (2004) have shown numerically that white noise inputs to a Hodgkin-Huxley neural network exhibits burst oscillations over a finite range of noise levels. Similar to our present results they found that increased noise strength produces increasing bursting frequency while decreasing the amplitude. Although, there are many differences between their model and ours, we find the qualitative agreement between the models suggestive of a deeper principle, namely, that large-N recurrent neural networks can exploit ensemble ergodicity, where fast synaptic transmission in the network computes an effective instantaneous average activity that is a shared input to every cell in the network in the noisy neural population, and slow AHP currents activate and deactivate based on long-time averaged activity. Oscillations exist in the network when the excitability of the cells, due to noise or a constant bias, is in a intermediate range, which is analogous to coherence resonance in other excitable neural systems (Lindner et al. 2004).

Our analytical and modeling study has potential applications to real biological neural networks. In the PreBotC slice preparation, extracellular potassium levels can be manipulated to control the existence and period of burst oscillations (Funk and Feldman 1995). Increase of extracellular potassium, which reduces the potassium outward leak current, thereby depolarizing the cell, could also increase the noisiness of the cellular environment.

For our two distinct AHP current models we have shown two distinct bifurcation mechanisms to oscillations that could have important consequences for burst rhythmogenesis. At the level of general single cell modeling it has been hypothesized that SNIC bifurcations in excitable membranes modeled as a relaxation oscillators can account for the high spiking irregularity and predict long latency to spiking from weak super-threshold depolarizing inputs, whereas Hopf instabilities exhibit more regular spiking and do not exhibit long post input latencies to spike (Gutkin and Ermentrout 1998). Furthermore, SNIC bifurcations exhibit an absolute threshold to spiking, whereas Hopf instabilities exhibit a "soft" ill-defined threshold to spiking. All of these theoretical results apply to our model because the spiking network reduces to a relaxation oscillator through the mean-field approximation in the large–N limit. This suggests that examining the behavior of the spiking and mean-field systems to transient inputs or abrupt parameter changes could generate experimental predictions regarding PreBotC burst rhythmogenesis. Of course, with a large network the oscillations are quasi–deterministic and very regular. In a smaller network however, more irregular population burst patterns can be observed. These irregular activity patterns are similar to up and down states observed in cortical slices (see McCormick and Yuste 2006, for a review). Up-states (high activity) and Down states (low activity) in cortex are thought to be due to recurrent excitatory network ensembles that exhibit transient up and down episodes. Such episodes can be toggled by inputs, and stochastic forces ostensibly produce the random-like switching observed in slice work. Recently, noise driven mean-field equations of up–down dynamics have been studied (Holcman and Tsodyks 2006). While the present work does not explore finite–N fluctuations, our model could be adapted to study such up–down phenomena.

Acknowledgements This work was supported by the NSF (DMS 0515725 and RTG 0354259). The authors would also like to thank Christopher Del Negro and Peter Roper for their helpful suggestions and comments.

References

Brockhaus, J., & Ballanyi, K. (1998). Synaptic inhibition in the isolated respiratory network of neonatal rats. *European Journal of Neuroscience, 10*, 3823–3839.

Butera, R. J., Rinzel, J., & Smith, J. C. (1999a). Models of respiratory rthythm generation in the pre-bötzinger complex. I. bursting pacemaker neurons. *Journal of Neurophysiology, 81*, 382–397.

Butera, R. J., Rinzel, J., & Smith, J. C. (1999b). Models of respiratory rthythm generation in the pre-bötzinger complex. II. Populations of coupled pacemaker neurons. *Journal of Neurophysiology, 81*, 398–415.

Buzaki, G. (2007). *Rhythms in the brain*. Oxford: Oxford University Press.

Chub, N., & O'Donovan, M. J. (2001). Post-episode depression of GABAergic transmission in spinal neurons of the chick embryo. *Journal of Neurophysiology, 85*, 2166–2176.

Cupello, A. (2003). Neuronal transmembrane chloride electrochemical gradient: A key player in GABAA receptor activation physiological effect. *Amino Acids, 24*, 335–346.

Del Negro, C. A., Johnson, S. M., Butera, R. J., & Smith, J. C. (2001). Models of respiratory rthythm generation in the pre-bötzinger complex. III. Experimental tests of model predictions. *Journal of Neurophysiology, 86*, 59–74.

Del Negro, C. A., Morgado-Valle, C., & Feldman, J. L. (2002). Respiratory rhythm: An emergent network property? *Neuron, 34*, 821–830.

Destexhe, A., Rudolph, M., Fellous, J. M., & Sejnowski, T. J. (2001). Fluctuating synaptic conductances recreate *in vivo*-like activity in neocortical neurons. *Neuroscience, 107*, 13–24.

Feldman, J. L., & Del Negro, C. A. (2006). Looking for inspiration: New perspectives on respiratory rhythm. *Naturalist Reviews in Neuroscience, 7*, 232–242, March.

Funk, G. D., & Feldman, J. L. (1995). Generation of respiratory rhythm and pattern in mammals: Insights from developmental studies. *Current Opinion in Neurobiology, 5*, 778–785.

Gang, H., Ditzinger, T., Ning, C. Z., & Haken, H. (1993). Stochastic resonance without external periodic force. *Physical Review Letters, 71*, 807–810.

Gardiner, C. W. (2004). *Handbook of stochastic methods*. New York: Springer.

Ge, Q., & Feldman, J. L. (1998). AMPA receptor activation and phosphatase inhibition affect neonatal rat respiratory rhythm generation. *Journal of Physiology, 509*, 255–266.

Gigante, G., Mattia, M., & Giudice, P. D. (2007). Diverse population-bursting modes of adapting spiking neurons. *Physical Review Letters, 98*, 148101.

Gutkin, B. S., Ermentrout, B. G. (1998). Dynamics of membrane excitability determine inter-spike interval variability: A link between spike generation mechanisms and cortical spike train statistics. *Neural Computation, 10*, 1047–1065.

Han, S. K., Yim, T. G., Postnov, D. E., & Sosnovtseva, O. V. (1999). Interacting coherence resonance oscillators. *Physical Review Letters, 83*, 1771.

Hille, B. (2001). *Ion channels of excitable membranes, 3rd edition*. Sunderland, MA: Sinauer.

Holcman, D., & Tsodyks, M. (2006). The emergence of up and down states in cortical networks. *PLoS Computational Biology, 2*(3), 0714–0181.

Izhikevich, E. M. (2007). *Dynamical systems in Neuroscience: The geometry of excitability and bursting*. Cambridge: MIT.

Johnson, S. M., Wilkerson, J. E., Wenninger, M. R., Henderson, D. R., & Mitchell, G. S. (2002). Role of synaptic inhibition in turtle respiratory rhythm generation. *Journal of Physiology, 544*, 253–265.

Jonas, E., & Kaczmarek, L. K. (1999). The inside story: Subcellular mechanisms of neuromodulation. In P. S. Katz (Ed.), *Beyond neurotransmission: Neuromodulation and its importance for information processing* (pp. 83–120). Oxford: Oxford University Press.

Kosmidis, E. K., Pierrefiche, O., & Vibert, J. F. (2004). Respiratory-like rhythmic activity can be produced by an excitatory network of non-pacemaker neuron models. *Journal of Neurophysiology, 92*, 686–699.

Kurrer, C., & Schulten, K. (1995). Noise-induced synchronous neural oscillations. *Physical Review E, 51*, 6213.

Kuznetsov, Y. A. (2004). *Elements of Applied Bifurcation Theory, 3rd edition*. New York: Springer-Verlag.

Lindner, B., Garcia-Ojalvo, J., Neiman, A., & Schimansky-Geier, L. (2004). Effects of noise in excitable systems. *Physics Reports, 392*, 321–424.

Loebel, A., & Tsodyks, M. (2002). Computation by ensemble synchronization in recurrent networks with synaptic depression. *Journal of Comparative Neuroscience, 13*, 111–124.

Mattia, M., & Giudice, P. D. (2002). Population dynamics of interacting spiking neurons. *Physical Review E, 66*, 051917.

McCormick, D. A., & Yuste, R. (2006). Up states and cortical dynamics. In G. Grillner (Ed.), *Microcircuits: The interface between neurons and global brain function*. Cambridge: MIT.

O'Donovan, M. J. (1999). The origin of spontaneous activity in developing networks of the vertebrate nervous system. *Current Opinion in Neurobiology, 9*, 94–104.

Pace, R. W., Mackay, D. D., Feldman, J. L., & Del Negro, C. A. (2007). Role of persistent sodium current in mouse pre-Bötzinger complex neurons and respiratory rhythm generation. *Journal of Physiology, 582*, 485–496.

Pham, J., Pakdaman, K., & Vibert, J. F. (1998). Noise-induced coherent oscillations in randomly connected neural networks. *Physical Review E, 58*, 3610.

Pikovisky, A., & Ruffo, S. (1999). Finite-size effects in a population of interacting oscillators. *Physical Review E, 59*, 1633.

Pradines, J. R., Osipov, G. V., & Collins, J. J. (1999). Coherence resonance in excitable and oscilatory systems: The essential role of slow and fast dynamics. *Physical Review E, 60*, 6407.

Rappel, W. J., & Karma, A. (1996). Noise-induced coherence in neural networks. *Physical Review Letters, 77*, 3256.

Rappel, W. J., & Strogatz, S. (1994). Stochastic resonance in an autonomous system with a nonuniform limit cycle. *Physical Review E, 50*, 3249–3250.

Rinzel, J., & Ermentrout, B. (1998). Analysis of neural excitability and oscillations. In C. Koch, I. Segev (Eds.), *Methods of neuronal modeling: From synapses to networks, 2nd Ed.* (pp. 252–291). Cambridge: Bradford.

Sernagor, E., Chub, N., Ritter, A., & O'Donovan, M. J. (1995). Pharmacological characterization of the rhythmic synaptic drive onto lumbosacral motoneurons in the chick embryo spinal cord. *Journal of Neuroscience, 15*, 7452–7464.

Shelly, M. J., & Tao, L. (2001). Effidient and accurate time-stepping schemes for integrate-and-fire neuronal networks. *Journal of Comparative Neuroscience, 11*, 11–119.

Smith, J. C., Ellenberger, H. H., Ballanyi, K., Richter, D. W., & Feldman, J. L. (1991). Pre-Bötzinger complex: A brainstem region that may generate respiratory rhythm in mammals. *Science, 254*, 726–729.

Tabak, J., O'Donovan, M. J., Rinzel, J. (2006). Differential control of active and silent phases in relaxation models of neuronal rhythms. *Journal of Comparative Neuroscience, 21*, 307–328.

Tabak, J., & Rinzel, J. (2005). Bursting in excitatory neural networks. In S. Coombes & P. C. Bressloff (Eds.), *Bursting: The genesis of rhythm in the nervous system* (pp. 273–301). Hackensack: World Scientific.

Tabak, J., Rinzel, J., & O'Donovan, J. (2001). The role of activity-dependent network depression in the expression and self-regulation of spontaneous activity in the developing spinal cord. *Journal of Neuroscience, 21*, 8966–8978.

Tabak, J., Senn, W., O'Donovan, J., & Rinzel, J. (2000). Modeling of spontaneous activity in developing spinal cord using activity-dependent depression in an excitatory network. *Journal of Neuroscience, 20*, 3041–3056.

Tryba, A. K., Peña, F., & Ramirez, J. M. (2003). Stabilization of bursting in respiratory pacemaker neurons. *Journal of Neuroscience, 23*, 3538–3546.

Tsodyks, M., Uziel, A., & Markram, H. (2000). Synchrony generation in recurrent networks with frequency-dependent synapses. *Journal of Neuroscience, 20*, RC50.

Van Vreeswijk, C., & Hansel, D. (2001). Patterns of synchrony in neural networks with spike adaptation. *Neural Computation, 13*, 959–992.

Vladimirski, B. B., Tabak, J., O'Donovan, M. J., & Rinzel, J. (in press). Episodic activity in a heterogenious excitatory network, from spiking neurons to mean field. *Journal of Comparative Neuroscience*.

Wilson, H. R., & Cowan, J. D. (1972). Excitatory and inhibitory interactions in localized populations of model neurons. *Biophysical Journal, 12*, 1–22.